Quantification of impurities in diatomite via sensitivity-improved calibration-free laser-induced breakdown spectroscopy

Nabila Belkhir, Sid Ahmed Beldjilali, Mohamed Amine Benelmouaz, Saad Hamzaoui, Anne-Patricia Alloncle, Christoph Gerhard, Jörg Hermann

Quantification of impurities in diatomite via sensitivity-improved calibration-free laser-induced breakdown spectroscopy

Nabila Belkhir[1,2], Sid Ahmed Beldjilali[1,*], Mohamed Amine Benelmouaz[1], Saad Hamzaoui[2], Anne-Patricia Alloncle[3], Christoph Gerhard[4] and Jörg Hermann[3]

[1]*Laboratoire de Physique des Plasmas, Matériaux Conducteurs et leurs Applications LPPMCA, Université des Sciences et de la Technologie d'Oran Mohamed Boudiaf USTO-MB, BP 1505 El M'naouer, 31000 Oran, Algeria*

[2]*Laboratoire de Microscopie Electronique & Sciences des Matériaux, Université des Sciences et de la Technologie d'Oran Mohamed Boudiaf USTO-MB, BP 1505 El M'naouer, 31000 Oran, Algeria*

[3]*Aix-Marseille University, CNRS, LP3, 13288 Marseille, France*

[4]*Fakultät für Ingenieurwissenschaften und Technik, Hochschule für angewandte Wissenschaft und Kunst, Von-Ossietzky-Straße 99, 37085 Göttingen, Germany*

*Corresponding author: sidahmed.beldjilali@univ-usto.dz

Abstract

The detection of impurities in diatomite is a critical issue during the silicon extraction process. Impurities can significantly impact the properties of silicon, compromising the performance of Si solar cells. In the present work, we applied a sensitivity-improved calibration-free LIBS measurement approach to assess the quality of diatomite. Based on the recording of two spectra with different delays between the laser pulse and the detector gate, the method enables the quantification of major, minor, and trace elements. The limits of detections for minor and trace elements were evaluated. Furthermore, we investigated the morphology and properties of the diatomite surface using Energy-Dispersive X-ray Spectroscopy and Scanning Electron Microscopy analysis. This research contributes to process optimization in the fabrication of electronic grade silicon from diatomite for photovoltaic technology and other applications.

Keywords: Diatomite, Elemental analysis, LIBS, Calibration-free, Limits of detection, SEM, EDX.

1 Introduction

Solar power is a natural and cost-free resource provided by nature to fulfill life's needs. There has been substantial progress in this technology to enhance solar cell efficiency and decrease manufacturing expenses[1, 2]. Silicon is a key player in this field[1], but the increasing demand for it has raised concerns about its limited reserves. As a result, the quest for alternative solutions to address this challenge has begun.

In this context, the environment offers a solution, especially through the presence of phytoplankton species, particularly diatoms. They are responsible for forming siliceous rocks due to their significant 50% contribution to photosynthesis[3-5]. By harnessing this natural resource, an essential skill emerges in the search for sustainable solutions to meet the increasing demand for silicon while preserving the environment[6].

The extraction of high-purity silicon from diatoms is crucial due to the detrimental effects of impurities on the efficiency of silicon-based solar cells. Impurities can impair the conversion of light into electricity by inducing carrier recombination as result of the reduced minority carrier lifetime and diffusion length[7, 8]. Moreover, elevated levels of contamination can disrupt voltage and current, leading to a decline in the

fill factor and overall efficiency of solar cells[9]. Additionally, heightened crystalline defects or an abundance of impurities can interfere with the crystallographic structure, fostering the formation of defects such as grain boundaries and dislocations, which in turn trap charge carriers[8]. These factors can potentially compromise the performance of solar cells produced from silicon.

Once impurities are detected, purification procedures can be implemented to eliminate or reduce their presence in diatomite. Common techniques used for diatomite purification include acid washing[10], thermo-chemical treatments[11] and microwave radiation processes[12]. Maintaining low impurity levels in diatomite is crucial to guarantee the effectiveness of silicon production.

Various physico-chemical and mineralogical analysis techniques can be employed to detect impurities. Among these methods are traditional analytical techniques such as Fourier Transform Infrared Spectroscopy (FTIR)[13], which is used to identify chemical bonds and molecular vibrations in the sample. X-ray Photoelectron Spectrometry (XPS)[14] analysis is utilized to characterize surface composition, while trace element analysis can be performed using techniques such as Atomic Absorption Spectrometry (AAS)[15], Inductively Coupled Plasma Mass Spectrometry (ICP-MS)[16], and Inductively Coupled Plasma Optical Emission Spectrometry (ICP-OES)[17]. The latter was for example used in collaboration between Japanese and Algerian groups to monitor the composition of solar-grade silicon during the extraction process[17]. Additionally, Scanning Electron Microscopy (SEM) [16] coupled with Energy-Dispersive X-ray (EDX) microanalysis was employed to visualize surface morphology and track elemental distributions within the diatomite surface. Moreover, X-ray Diffraction (XRD) is utilized to characterize the crystalline structure of materials, including diatomite[16].

Thorough monitoring of the kinetics of the silicon raw material purification process is essential to ensure efficiency. It is crucial to choose a more advanced analysis method than classical elementary analysis methods, which have limitations in monitoring the evolution of this process. Laser-induced breakdown spectroscopy has attracted growing interest [18, 19], positioning it as a promising method for quality control of diatomite. The technique enables real-time analysis without prior sample preparation and with minimal sample destruction[18, 19]. This method relies on generating plasma using a laser, and by analyzing the radiation emitted from the plasma, enabling the identification of sample constituents through their emission wavelengths and their concentration via intensity measurements[18, 19].

As in other analytical methods, quantification via LIBS relies usually on constructing calibration curves. This process involves measuring the emission intensity of a spectral line across various reference samples with different concentrations, plotting the intensity against the concentration. However, calibration faces significant challenges, including non-linearity due to line intensity saturation as a consequence of self-absorption[20-22], and variations in material response to laser irradiation, resulting in matrix effects associated to fluctuations of the ablated sample volume and the plasma temperature. Despite attempts to mitigate these issues, the precision of quantification remained limited, requiring prior knowledge of the elemental composition of standard samples and incurring substantial time and resource costs.

To address these limitations, calibration-free LIBS has been developed. This method avoids the need to create calibration curves, providing benefits such as rapid analysis and elimination of sample preparation. Its fundamental principle, introduced by Ciucci *et al.* in 1999[23], is based on the assumptions of local thermodynamic equilibrium (LTE), plasma uniformity, stoichiometric ablation, and optically thin plasma emission. The correlation between light intensity and emission coefficient facilitates the determination of mass fraction via a simple Boltzmann plot[18]. However, the effect of self-absorption, which is inherent to local thermodynamic equilibrium plasmas, reduces the analytical performance[24]. Thus, methods have been developed to compensate for self-absorption in calibration-free LIBS analysis [25-27]. In our work, we use a calibration-free approach[28] that is based on the analytical solution of the radiation transfer equation for a spatially uniform LTE plasma[29]. This approach intrinsically accounts for self-absorption. Implemented in an appropriate iteration loop of consecutive electron density, temperature, and elemental fraction measurements[30], accurate analysis can be operated for the entire sample composition including major, minor and trace elements[31, 32].

Diatomite presents a complex matrix featuring elements with large energy gaps in their atomic structure, for which the Boltzmann equilibrium distribution of population number densities is hardly achieved. We therefore employ a sensitivity-improved calibration-free approach using distinct spectra measurements for the quantification of major, minor and trace elements, respectively[32, 33] . We evaluate the detection limits of minor and trace elements to optimize the sensitivity of our technique.

Furthermore, we investigate the morphology of diatomite using scanning electron microscopy and conduct quantitative energy-dispersive X-ray analysis. These complementary space-resolved analyses provide information on the fluctuation of elemental fraction on a microscopic scale. The objective here is not to directly analyze the quantitative measurements given by EDX, but to compare the results obtained with the same measurement method on different areas of the same sample.

2 Materials and methods

2.1 Experimental details

2.1.1 Experimental setup

As sample material, a diatomite stone was collected from the Sig region (KIESELGUHR, Tahalait deposit) in north-west Algeria and was subsequently cut into several cubes of 1 cm³ volume and 1.5 g mass.

The LIBS experiments were performed using ultraviolet (266 nm) Nd:YAG laser pulses of 4 ns duration and 6 mJ energy [see Fig. 1]. The laser beam is focused onto the sample surface using a plano-convex lens with a focal length of 150 mm, resulting in a fluence of approximately 80 J cm^{-2}. The samples are placed on a motorized *xyz* linear stage mounted inside a vacuum chamber with a residual pressure of 10^{-5} Pa, filled with argon at a pressure of 5×10^4 Pa. The laser-induced plasma emission is captured by a condensing optical system consisting of two lenses of 150 and 37.5-mm focal lengths coupled into a multimode optical fiber with a core diameter of 600 µm. The optical fiber is connected to an echelle spectrometer (LTB, model Aryelle Butterfly) with a resolving power of 1×10^4 equipped with an intensified charge-coupled device (ICCD) detector (Andor, model IStar) for time-resolved spectral recordings.

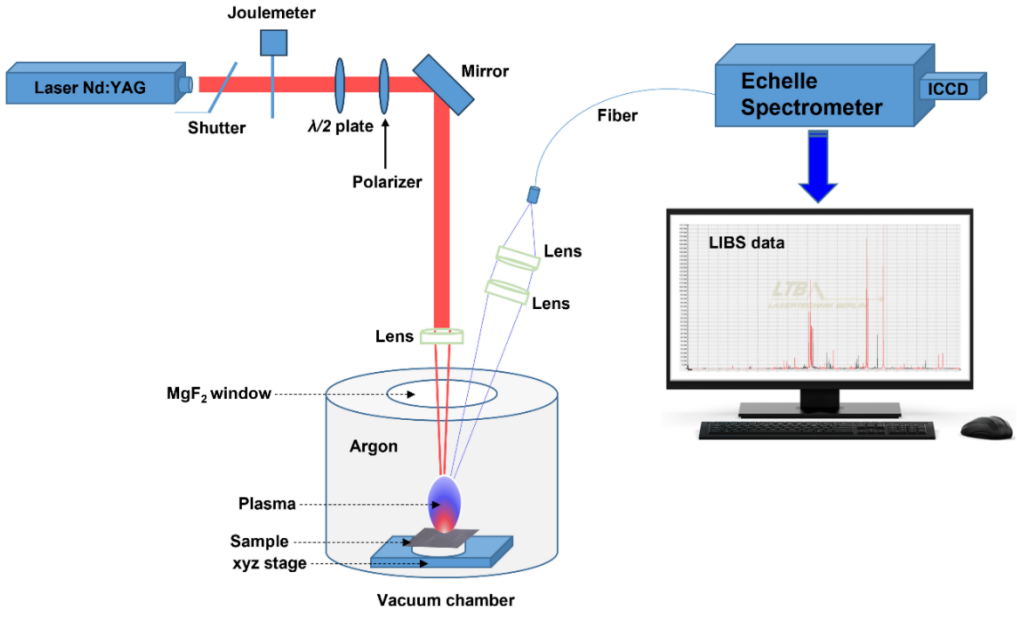

Fig. 1 Experimental setup for LIBS measurements.

The spectra were recorded with delays of the detector gate with respect to the laser pulse t_{delay} = 400 ns and 1000 ns. The gate width Δt_{gate} was chosen to $\Delta t_{gate} = t_{delay}/2$ as a compromise between the smallest available variation of plasma properties during the time of observation and the highest reachable signal-to-noise ratio[34]. The data acquisition was performed by averaging over 480 ablation events, irradiating 160 sites on the sample surface with 3 laser pulses each. The sites were separated by a distance of 150 µm.

2.1.2 Sensitivity-improved calibration-free LIBS measurements

To enable analysis of major-, minor-, and trace elements, we performed sensitivity-improved calibration-free LIBS measurements based on a previously introduced "two-step procedure" [33]. This method is based on the recording of two spectra at different delays after the laser pulse.
The early recording is operated when the electron density is large enough to ensure full LTE conditions. According to the moderate signal-to-noise ratio, only major and minor elements can be quantified in this condition[33].
The late recording is operated to achieve the highest signal-to-noise ratio necessary for detecting trace elements. At this stage, the plasma is in a state of partial equilibrium, where the matrix elements with large energy gaps (C, H, O) are out of equilibrium, while the other plasma species still have Boltzmann equilibrium distributions. These conditions favor the quantification of minor and trace elements.

2.2 Sample characterization via SEM and EDX analysis

The morphological structure of the diatomite surface was investigated with a field emission scanning electron microscope (JEOL, model JSM 6390) that was operated with an electron beam voltage of up to 20 kV. The atomic fractions of the elements constituting the diatomite were measured using energy-dispersive X-ray spectroscopy (JEOL, model JSM 6390). Prior to the analysis, a 1.5 g cubic sample of diatomite was subjected to high vacuum conditions under pressure of 10^{-5} torr using a vacuum coating system (BOC Edwards, model Auto306) for a duration of 30 minutes to ensure the elimination of any moisture-related effects. Subsequently, a thin layer of gold with a thickness of 10 nm was deposited using a coating system (JEOL, model Smart coater JEOL_781186455) to limit any charging effects during measurement.

3 Results and discussion

3.1 Microscopic analysis

3.1.1 SEM observation of surface morphology

Diatomaceous deposits in Algeria formed during the Miocene era, as continental formations emerged. This period was marked by intense volcanic activity, which brought in a significant reserve of silica, essential for creating diatomite[35]. Diatoms, single-celled microorganisms, accumulated in lake environments, creating sedimentary deposits rich in siliceous frustules. The polycondensation process of dissolved silica resulted in the formation of diatom silica frustule[36], presenting a regular structure essential for various industrial uses.

In order to examine these varieties of frustules present in diatoms and their potential impact in the photovoltaic field, we chose to use high scanning electron microscopy analysis. Through this analysis, we discovered a complex structure within the surface morphology of diatom earth, encompassing a variety of shapes with dimensions ranging from a few hundred nanometers to a few hundred microns [see Fig. 2 (a)]. These shells, called diatom frustules, have radial symmetry and are generally cylindrical and centered in shape[36]. They are characterized by valve ornaments arranged in the axial direction, as well as numerous pores, cavities and microscopic rings corresponding to the biogenic silica skeleton [see Fig. 2 (b)][36].

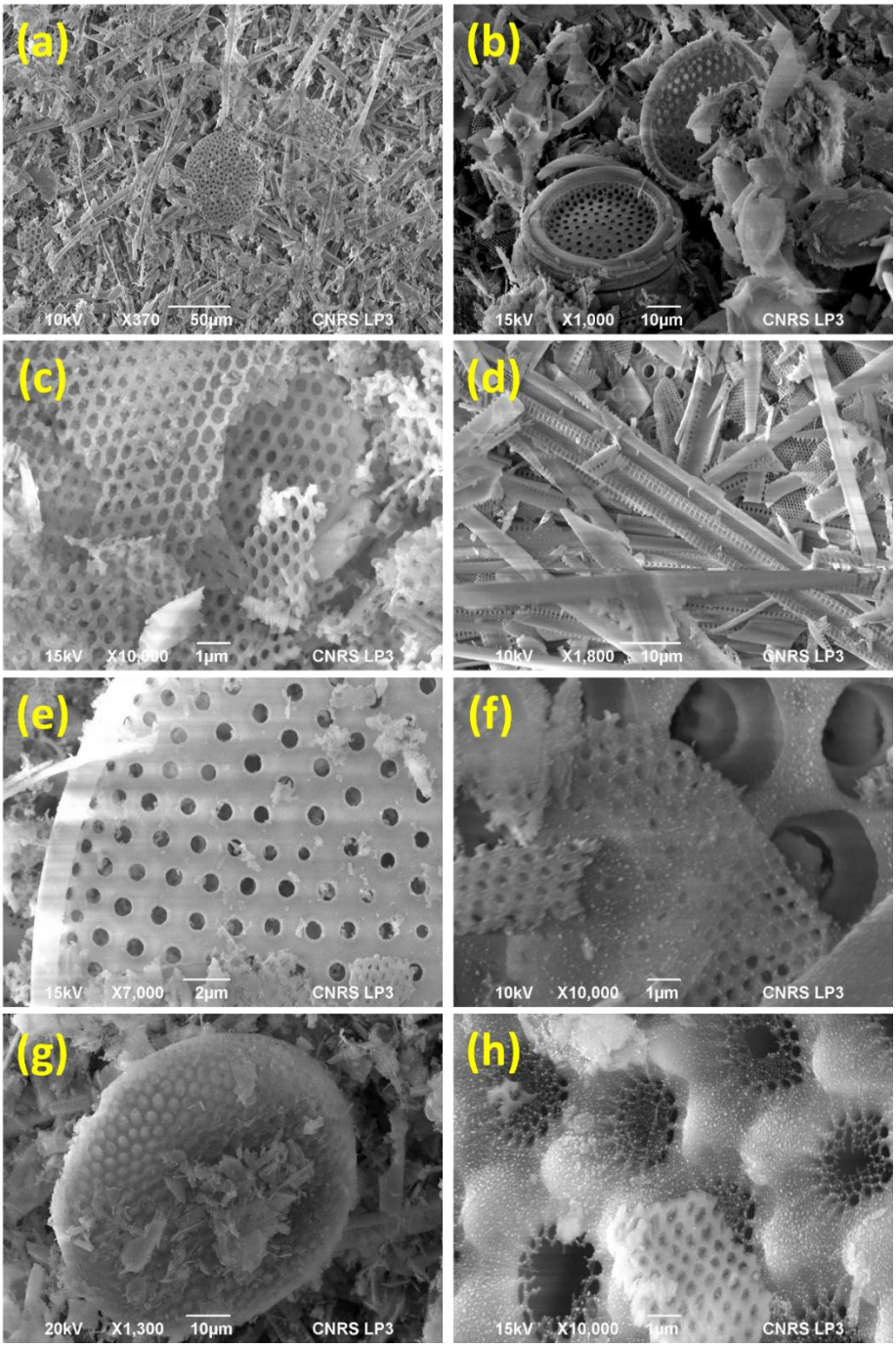

Fig. 2 (a)-(h) Morphology of different diatomite species examined by SEM.

Fig. 2 (c) shows a configuration similar to a fishing net with significant potential as a filter, capable of capturing particles of various sizes according to their dimensions. In addition, Fig. 2 (d) presents an additional type of diatom, the filamentous diatom[37], characterized by a tubular structure with fine pores along its margins.

In Fig. 2 (e), we observe a crystalline structure serving as a diffraction network, effectively guiding light along the diatom's axis. In parallel Fig. 2 (f), we observe the superposition of three layers within a hexagonal lattice, featuring a porosity ranging from micrometer-scale inside to a nanometer-scale average, with even smaller pores at the nanometer level on the exterior, which is coated with a thin layer [see Fig. 2 (g)] of silica known as the cribellum layer, punctuated with flower-shaped pores, as depicted

in Fig. 2 (h)[38]. Examination of these frustules clearly reveals the micro-/nano-hierarchical structure of diatoms, comprising three layers (foramen, cribrum, cribellum) organized in hexagonal arrangements[38, 39]. This architecture holds exceptional potential for photonic applications, enabling diatoms to efficiently capture light through constructive interferences resulting from multiple layers of diffusion[38].

Moreover, their regular arrangement of pores in superimposed layers, according to a hierarchically ordered periodic pattern, gives diatoms a characteristic of living photonic crystals[40]. The use of their silica shells as light traps is highly desirable and can be exploited on a large scale to create natural nanostructured layers for photovoltaic devices[41]. Following this approach, after the extraction, characterization, and functionalization of the shells, prior studies propose processes for integrating the bio silicon into simple devices for the production of solar energy. For example, Sun *et al*.[38] used diatom frustules to create a solar capture layer on the surface of a thin solar cell layer, thus increasing light absorption by simply exploiting silica nanostructures. On the other hand, Raston and his team[42] coated the diatoms with TiO_2 nanoparticles to produce biosilicon-based in dye-sensitized solar cells, thereby increasing solar energy conversion efficiency by 30%. The abundance of silica in the diatomite phase attracts the attention of researchers who plan to explore its potential use in the manufacture of solar-grade silicon [10, 12, 17, 43, 44].

The presence of diverse pores in diatomite and the intricate construction of its frustules at room temperature serve as motivations for scientists to unravel the fundamental elements that constitute diatomite. In this pursuit, we used several analytical techniques, including Energy Dispersive X-ray Spectroscopy and Laser-Induced Breakdown Spectroscopy. EDX enables the spatial identification of various constituents on the surface, while LIBS offers a new avenue for detecting and quantifying elements in diatomite. By employing the synergistic combination of EDX and LIBS techniques in this study, we can attain a comprehensive understanding of the elemental composition of diatomite.

3.1.2 Spatially resolved compositional analysis via EDX

EDX analysis was conducted across various regions on the sample's surface [see Fig. 3] to investigate the spatial distribution of impurities and to determine the mean concentration of elements within 13 distinct zones, thus assessing their presence throughout the surface.

The qualitative analysis of the spectrum obtained by EDX reveals that the predominant composition of all types of frustules is silica, although the amount of impurities may vary depending on the type of frustule. Additionally, the porous structure of diatomite (zone 2, 3, and 5) can act as trapping centers for contaminants.

According to the elemental fractions measured via EDX within 13 distinct zones (see Table 1), the diatomite is composed of silica and several other minerals fluctuating concentrations. The presence of these minerals can be attributed to various sources, such as the environmental conditions in which diatoms thrive or the geological processes involved in the formation of diatomite.

The standard deviation (see Table 1) and the distribution of impurities represented in Fig. 4 highlights a slight deviation from the mean for major elements such as silicon and oxygen, as well as for mineral impurities like sodium and aluminum. This suggests uniformity in their distribution on the surface of the diatomite. On the other hand, the detected trace elements exhibit significant variation, indicating heterogeneity in their distribution on the same surface of the diatomite.

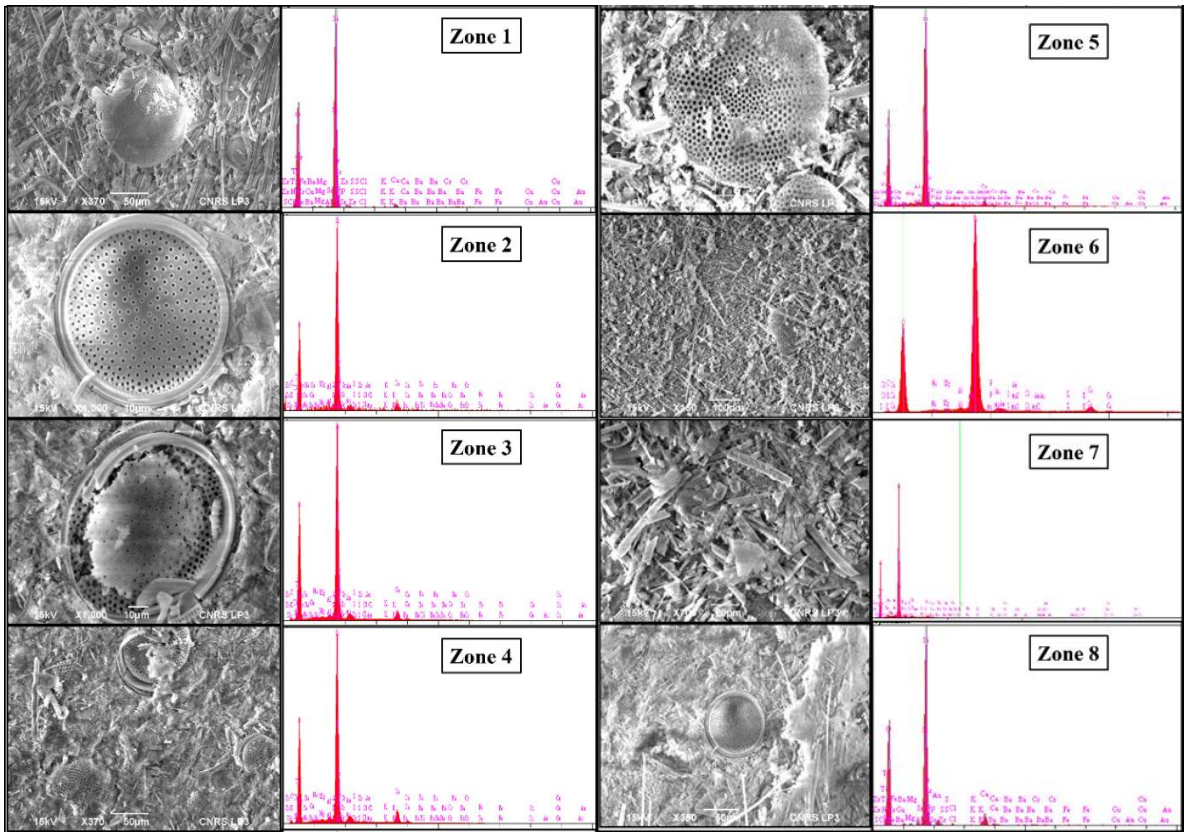

Fig. 3 In the left: different zones of diatomite analyzed by SEM. In the right: The spectra of different zones of diatomite obtained by EDX analysis.

Table 1 Mass fraction in % of the constituent elements of diatomite with standard deviation obtained through EDX analysis. Here, $\bar{x}$ is the mean value and *s* is the standard deviation.

Element	C	O	Na	Mg	Al	Si	K	Ca	Ti	Fe
Zone 1	1.79	50.8	0.35	0.22	0.51	42.23	0.061	3.83	0.05	0.15
Zone 2	2.29	48.5	0.39	0.41	0.85	41.58	0.12	5.5	0.03	0.33
Zone 3	2.33	45.34	0.49	0.301	0.52	47.65	0.69	2.3	0.085	0.301
Zone 4	2.2	45.71	0.36	0.26	0.51	48.13	0.11	2.37	0.05	0.28
Zone 5	0	47.18	0.58	0.54	0.48	45.84	0.304	3.48	0.23	1.38
Zone 6	1.43	49.04	0.29	0.24	0.43	47.19	0.083	0.98	0.034	0.28
Zone 7	2.15	47.06	0.803	0.42	0.59	44.83	0.19	3.55	0.082	0.32
Zone 8	1.11	45.21	0.94	0.105	0.25	51.6	0.085	0.48	0.025	0.18
Zone 9	0.77	44.55	0.302	0.070	0.27	53.16	0.19	0.48	0.04	0.15
Zone 10	0.86	45.18	0.302	0.05	0.24	52.78	0.15	0.302	0.025	0.11
Zone 11	1.025	46.25	0.402	0.13	0.35	50.82	0.201	0.67	0.027	0.12
Zone 12	0.93	44.18	0.302	0.037	0.26	53.54	0.14	0.41	0.058	0.14
Zone 13	0.946	45.79	0.34	0.109	0.33	51.47	0.19	0.59	0.014	0.21
$\bar{x}$	1.37	46.52	0.45	0.22	0.43	48.52	0.19	1.92	0.058	0.304
s	0.72	1.93	0.206	0.16	0.17	4.078	0.16	1.71	0.056	0.33

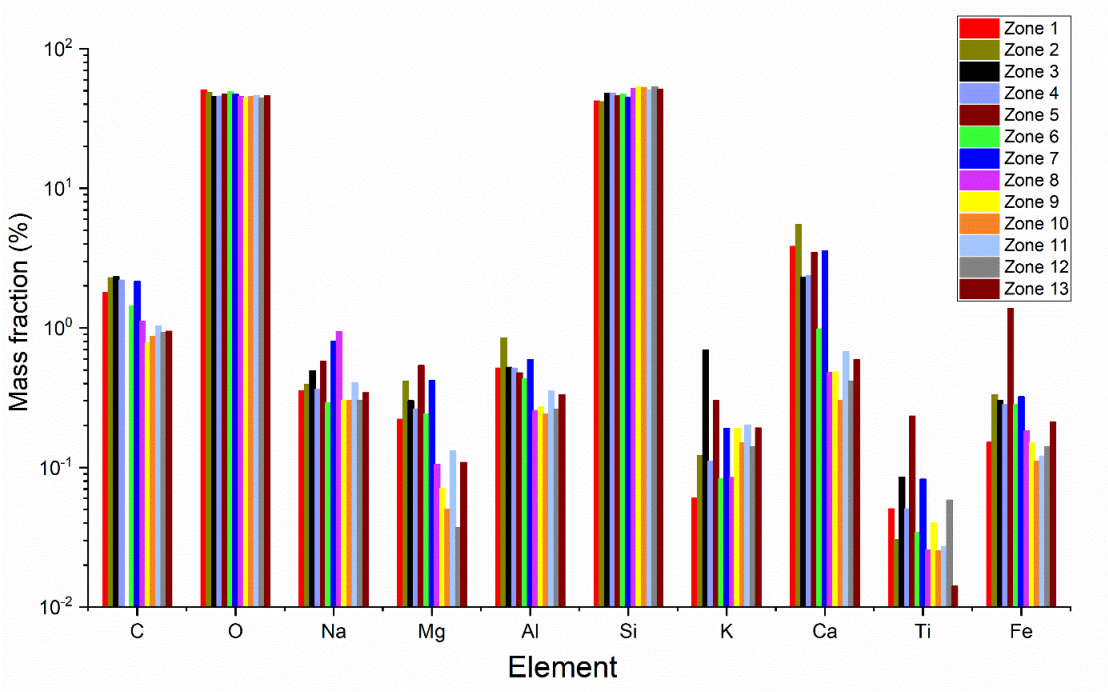

Fig. 4 The average mass fraction of the elements presents in diatomite in different zones by EDX analysis.

3.2 LIBS analysis

3.2.1 Qualitative analysis

3.2.1.a Selection of spectral lines

Table 2 presents the spectral lines utilized for quantifying major, minor, and trace elements, along with the accompanying data used for calculations. It is noteworthy that a significant portion of the Stark broadening parameters were acquired from a separate experiment, as documented in literature[45, 46]. Additionally, the signal-to-noise ratio is sufficiently high with low optical thickness (< 1), with no interference observed from lines of other elements. Moreover, reliable spectroscopic data are accessible.

Table 2 Transition probability A_{ul} with its accuracy $\Delta A_{ul}/A_{ul}$, energy E, statistical weight g of lower (index l) and upper (index u) electronic states, Stark broadening width w and shift d for n_e = 1×10^{17} cm^{-3} of lines used for compositional measurements. All the data were taken from NIST database[47].

Transition	A_{ul} (μs^{-1})	$\Delta A_{ul}/A_{ul}$(%)	E_l (ev)	g_l	E_u (ev)	g_u	w (pm)	d (pm)
Si I 390.55 nm	13.3	11	1.91	1	5.08	3	31[a]	16[a]
O I 777.19 nm	36.9	7	9.15	5	10.74	7	105	15
K I 769.89 nm	37.5	5	0	2	1.61	2	105	24
C I 247.86 nm	28	20	2.68	1	7.68	3	14	8.4
H I 656.29 nm	64.7	1	10.20	4	12.09	6	1109	80
Na I 589.59 nm	61.4	2	0	2	2.10	2	44	13
Al I 394.40 nm	49.9	5	0	2	3.14	2	42	24
Ca I 428.30 nm	43.4	20	1.89	3	4.78	5	41	-8.0
Fe II 274.93nm	216	10	1.04	6	5.55	8	5.0	0.0
Sr I 460.73 nm	201	2	0	1	2.69	3	31	3.5
Mg II 279.07 nm	401	7	4.42	2	8.86	4	30	9.0
Ti II 376.13 nm	120	7	0.57	6	3.87	6	15	-1.4
B I 249.77 nm	168	7	0	4	4.96	2	12	7
Li I 670.78 nm	36.9	1	0	2	1.85	4	39	-2.7
Cu I 324.75 nm	140	2	0	2	3.82	4	7.0[b]	3.0[b]

[a]Ref. [48], [b]Ref. [49].

The analysis of the LIBS spectrum reveals the presence of various elements, such as silicon, as well as mineral and clay impurities such as sodium, iron, calcium, magnesium, aluminum, and boron. These elements are detected through their specific spectral signatures, which are manifested by characteristic emission lines.

The recorded spectra for the early and late delays are displayed in Fig. 5 and 6, respectively.

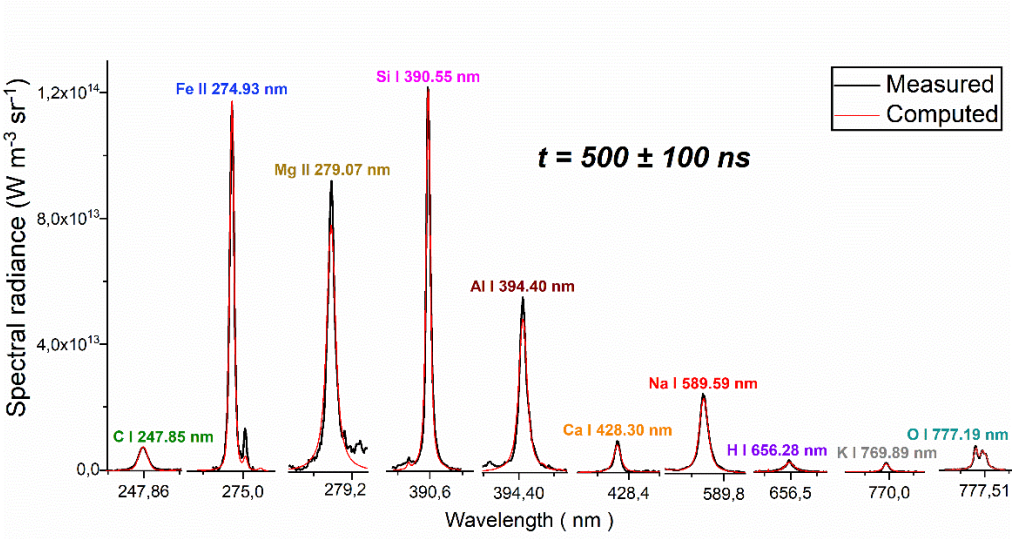

Fig. 5 The early spectrum is compared to the computed spectral radiance of a plasma in full LTE to deduce the fractions of major and most abundant minor elements.

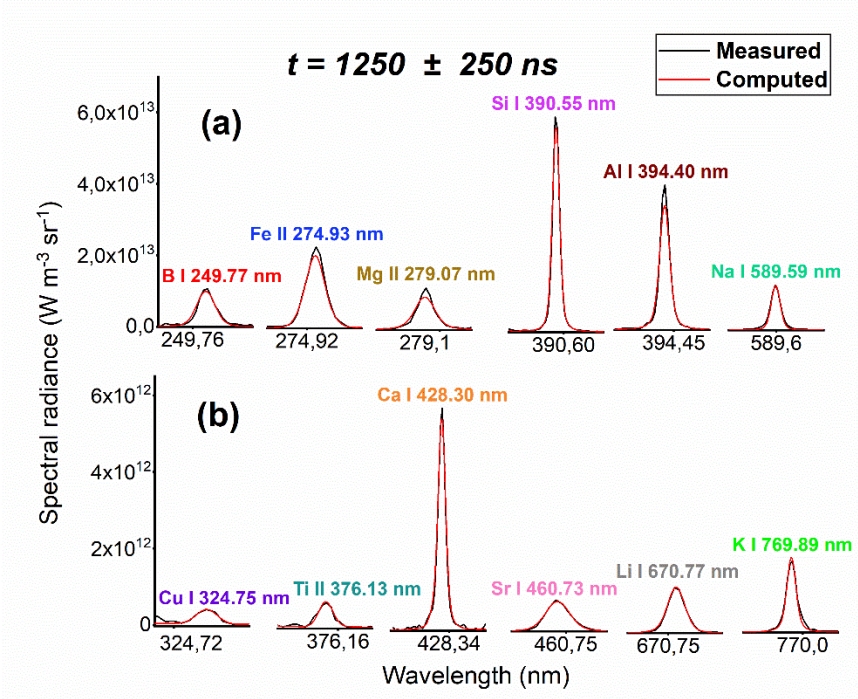

Fig. 6 (a) and (b) Late spectrum is compared to the computed radiance of a plasma in partial LTE to deduce the fractions of trace elements.

3.2.2 Quantitative analysis

3.2.2.1 Description of the LIBS Measurement Procedure

The relative fractions of the elements were determined using an iterative algorithm that estimates plasma properties by matching the calculated spectrum with the measured spectrum. This algorithm involves two iterative loops, as depicted in Fig. 7[32, 34].

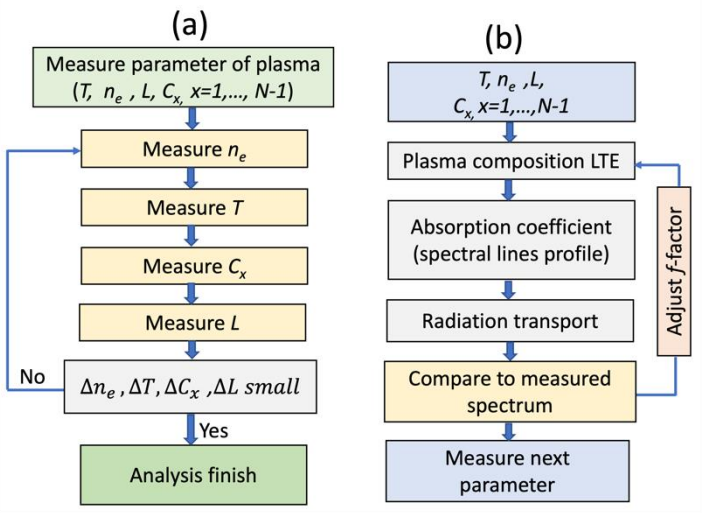

Fig.7 Overview of the main loop in the LIBS measurement procedure (a). Each measurement is conducted using the calculation Loop (b) with only the measured parameter being varied.

The main loop (a) involves successively measuring the parameters that describe the plasma, such as electron density, temperature, elemental fractions, and the size of the plasma along the observation direction. Each measurement is carried out using the calculation loop (b), which is employed to measure spectral radiance. The parameters are calculated by comparing the measured spectrum with the calculated spectrum and adjusting the parameter of interest until the best match is achieved. The relevant parameter is determined by minimizing the difference χ^2, as given by the following equation.

$$\chi^2(p) = \sum_i \frac{|f(p)B_i - I_i|^2}{I_i}, \quad (1)$$

Where B_i and I_i represent respectively the calculated and measured intensity values at point i, corresponding to the wavelength λ_i in the spectrum. The factor f is used to adjust the calculated spectrum to the measurements made and the index p represents the measured parameter.
The calculation of spectral radiance requires N-1+3 input parameters: the relative fractions of the N-1 elements, the temperature, the electron density and the dimensions of the plasma in the observation direction.
The main loop (a) begins with arbitrary values: n_e = 10^{17} cm^{-3}, T = 10^4 K, L = 0.5 mm, and equal elemental concentrations. Initially, the electron density is inferred by analyzing the Stark broadening of an appropriate spectral line. through the calculation of the theoretical spectrum varying n_e. The factor f_{ne} (see equation (1)) is adjusted to minimize χ^2 between the calculated and measured intensity at the line center, thereby determining the optimal value of n_e.

Subsequently, the plasma temperature is determined from the relative intensities of the spectral lines of the major element. Similar to the method used to determine the electron density, the temperature is derived by calculating the spectrum while systematically varying the temperature T so that the calculated spectrum agrees with the measured spectrum.

After measuring the temperature, the relative fractions of elements are adjusted. The normalization factor f determined by matching the calculated intensity to the measured intensity of the spectral line corresponding to the major element. Subsequently, for the remaining $N-1$ elements, elemental fractions are successively adjusted to minimize χ^2 for each measured spectral line compared to the calculated spectrum. This adjustment process continues until the χ^2 measurement becomes small.
In the final phase of the iteration, the dimensions of the plasma are determined using the intensity ratio between two resonance lines with significantly different optical thicknesses, which are in the same transition state. The parameter L is deduced by minimizing the χ^2 deviation between the measured and calculated spectra.
A new iteration is then initiated (see Fig.7) using the actual values of the electron density, temperature, relative elemental fractions, and plasma dimensions. During the second iteration, the precision of the electron density measurement is improved, as the spectral radiance calculation is now performed with more accurate values of temperature and elemental fractions, leading to a more precise optical thickness. The iteration continues until the variation in the parameters Δn_e, ΔT, ΔC_x and ΔL become insignificant compared to their absolute values.
For each measurement, the electron density is deduced from the Stark broadening of the Si I 390 nm transition[48], while the temperature is deduced from the relative intensities of silicon lines.

The values of electron density, temperature, plasma size, and elemental fraction deduced from the spectra measured at different times are shown in Table 3. The early spectrum is used to quantify the major elements and also hydrogen and carbon. In contrast, the late spectrum is used to quantify minor and trace elements such as sodium, iron, titanium, etc.

Table 3 Mass composition of diatomite constituents for the two considered delays (at 400ns and at 1000ns) measured via LIBS including EDX analysis results for comparison.

Measurement	**early**	**late**	**EDX**
t (µs)	0.5 ± 0.1	1.25 ± 0.25	
t_1 … t_2 *(µs)*	0.4 … 0.6	1.0 … 1.5	
n_e *(cm^{-3})*	(1.4 ± 0.3) × 10^{17}	(4.2 ± 1.6) × 10^{16}	
T (K)	10,900 ± 100	8,700 ± 200	
L (mm)	0.68	0.85	
O (%)	52.2 ± 5.2	-	46.52
Si (%)	38.0 ± 5.2	-	48.52
C (%)	2.1 ± 0.5	-	1.37
H (%)	0.68 ± 0.07	-	-
Ca (%)	3.0 ± 0.9	2.7 ± 0.7	1.92
Al (%)	1.36 ± 0.30	1.21 ± 0.30	0.43
Fe (%)	0.82 ± 0.14	0.94 ± 0.2	0.304
Mg (%)	0.66 ± 0.15	0.74 ± 0.14	0.22
K (%)	0.60 ± 0.18	0.72 ± 0.19	0.19
Na (%)	0.57 ± 0.10	0.66 ± 0.14	0.45
Sr (ppm)	-	503 ± 87	-
B (ppm)	-	352 ± 77	-
Ti (ppm)	-	273 ± 61	580
Li (ppm)	-	57 ± 9	-
Cu (ppm)	-	16 ± 5	-

The plasma size is determined by using the intensity ratio between two resonance lines with significantly different optical thicknesses that are in the same transition state, or through fast imaging of the ablation plume emission. In the present work, we use the ratio between the two sodium lines, Na I 588.99 nm and 589.59 nm.

The analysis of diatoms using LIBS show beside the presence of silicon and oxygen various minerals at concentrations ranging from 2% to parts per million (ppm). The uncertainty of the compositional

measurement was estimated according the error evaluation formalism proposed by Taleb et al.[22]. It is mainly due to the uncertainty of spectroscopic data, and to low signal-to-noise ratio in case of trace elements.

The uncertainty corresponds to LIBS spectra recording by signal accumulation over 480 laser ablation events. Thus, heterogeneities on a microscopic scale are ignored. They were investigated by the EDX analysis, and summarized by the standard deviations given in Table 1.

Both EDX and LIBS analyses confirm that diatomite is primarily composed of silica. However, it's important to note that in EDX analysis, placing the sample under vacuum to remove water molecules can alter the oxygen concentration, which in turn affects the measured silicon concentration.

Discrepancies between LIBS and EDX results can also be related to the differing extent of the sampled region, as both techniques, with their micrometric resolution, are not applied to exactly the same location on the sample surface. To clarify this point, attention was given to investigating the effect of surface inhomogeneity using SEM images. As shown in Fig. 3 for the diatomite sample, different elements constitute silicate minerals in various forms, most of which tend to be associated with frustules. In this case, the results of the current quantitative analysis can indeed be strongly dependent on the scanned region. However, sample inhomogeneity, as seen in diatomite, has been identified as a cause of discrepancies between different surface micro-analysis techniques[50]. To avoid this, results from a large number of measurements taken at different sample locations should be averaged over a much larger number of SEM electron beam than the value currently adopted for statistical optimization of EDX.

Additionally, Li and B are not detected by EDX due to the low sensitivity of this technique for detecting light elements[51]. This limitation makes EDX a semi-quantitative analysis technique[52]. Furthermore, the presence of pores can limit the detection of low-signal elements due to X-ray attenuation by air molecules[53].

The high concentration measurement of heavy elements by EDX in comparison to LIBS may be attributed to the limited penetration depth of electrons associated with these elements, influenced by interactions within the material or with other electrons. This interaction is mathematically described by the Kanaya and Okayama equation[54]. According to this equation, heavy elements tend to exhibit shorter electron ranges, leading to a faster loss of kinetic energy as they interact with the atoms of the material. Consequently, more intense electron emissions are observed near the surface of the material. This outcome could potentially affect the accuracy of EDX analysis, particularly in scenarios where there are variations in concentration between the surface and bulk of diatomite, which, being a rock, naturally exhibits different phases[55].

Moreover, the high heterogeneity of samples with different phases, such as diatoms, can affect EDX results because the radiation does not interact consistently across different regions[56].

In contrast, LIBS demonstrates a broader analytical capability. It can detect light elements such as boron lithium and hydrogen, in real-time and simultaneously capabilities that are less sensitive with EDX[51] and other analytical techniques. LIBS also shows superior detection sensitivity, capable of identifying elements at concentrations as low as a few dozen ppm, which is beyond the reach of EDX[53]. Furthermore, LIBS can analyze raw diatomite material without requiring any sample pretreatment, even with complex samples. This is a significant advantage over EDX, where the sample must be placed under vacuum to remove water molecules before analysis.

These results confirm the effectiveness of LIBS in detecting impurities in diatomite, while EDX analysis serves as a complementary method by providing information on surface homogeneity. The analysis of oxides in diatomite from different regions of the world via LIBS and other analytical methods (see Table 4) reveals several features. They indicate a rich silica content in Algerian diatomite from the Sig region, while the Ouled Djilali region in Algeria exhibits lower silica concentrations, attributed to silica reservoirs during rock sedimentation. Additionally, notable concentrations of K_2O, Na_2O, Al_2O_3, CaO, and Fe_2O_3 are observed in Algerian diatomite, possibly influenced by environmental properties such as humidity or water salinity, which promote salt concentration through evaporation, as well as fossil contamination during the rock formation process. Moreover, variations between different rock samples

can also be attributed to the specific layers being analyzed, as inconsistencies may arise during the deposition process of the rock.

In summary, the compositional differences in diatomite samples from various regions outline the intricate processes involved in their formation. The variations in silica content and elemental concentrations, particularly within Algerian diatomite, suggest nuanced environmental influences and sedimentary dynamics at play. Understanding these differences is crucial for interpreting the geological history and potential industrial applications of diatomite deposits worldwide.

Table 4 Mass composition of oxides in diatomite from different regions of the world via LIBS and other analytical methods.

Oxides	Algerian Diatomite "Sig region" (LIBS)	Algerian Diatomite "Sig region" (XRF)[17, 57, 58]	Algerian Diatomite "Ouled Djilali region"(XRF)[59]	Diatomite from different regions of the world (XRD, XRF, FP-AAS, ICP-MS)[60, 61]
SiO_2	81.2 %	[62.32- 82.36] %	[32.8-61.52] %	[62.8-91.84] %
CaO	3.8 %	[0.72- 7.2] %	[13.8-25.9] %	[0.1-10] %
Al_2O_3	2.3 %	[1.85-5.3] %	[3.44-5.7] %	[1.64-17.5] %
Fe_2O_3	1.3 %	[1.63-8.19] %	[1.5-2.26] %	[0.28 -11.4] %
MgO	1.2 %	[1.32-2.6] %	[0.4-3.14] %	[0.14-2.6] %
K_2O	0.87 %	[0.54-0.75] %	[0.49-0.84] %	[0.06-1.4] %
Na_2O	0.89 %	[0.65-1.12] %	[0.21-1.26] %	[0.06-7.3] %
SrO	0.059 %	-	[0.05-0.09] %	-
B_2O_3	0.11 %	-	-	-
TiO_2	0.045 %	[0.37-1.7] %	[0.17-0.29] %	[0.03-0.69] %
Li_2O	0.012 %	-	-	-
CuO	0.0019 %	-	-	-

To evaluate the sensitivity of detecting elements, present in diatoms, we conducted experimental measurements to determine the limit of detection under our specific experimental conditions.

3.2.3 Limit of detection LOD

The limit of detection of a chemical element is defined by the lowest concentration at which its intensity can be reliably distinguished from the background noise, typically set at three times the standard deviation of the noise ($3\sigma_{bg}$), using the formula[62]:

$$C_{LOD} = \frac{3\sigma_{bg}}{S}, \quad (2)$$

where S represents the sensitivity given by the slope of the calibration curve. The determination of the detection limit can be performed via calibration-free LIBS[63]. This involves several steps. Firstly, the most intense spectral lines are selected while ensuring no interference from other peaks. Subsequently, the spectrum of a trace element is computed for the given, previously determined plasma properties. For each chosen spectral line, the background noise is analyzed by conducting a normal distribution analysis and calculating the standard deviation σ_{bg}. The growth curve is established by computing the intensity of the analytical line as a function of the elemental fraction. The limit of detection is given by the mass fraction for which the line intensity reaches $3\sigma_{bg}$. This method enables the determination of the detection limit even for elements for which no spectral line was observed. It only requires the

spectroscopic data for the calculation of spectrum emitted by the element, and the measured spectrum to quantify the background signal fluctuation[63].

Sensitivity enhancement via the LIBS technique requires optimization of experimental parameters such as laser energy, recording time, detection sensitivity, etc. By taking these elements into account, it is possible to obtain reliable detection limit measurements for elemental analysis by LIBS.

Fig. 8 presents the detection limits of the elements detected in diatomite using the LIBS method. It can be observed that the majority of elements exhibit detection limits ranging from 2 to 50 ppm. The lower sensitivity observed for certain elements can be attributed to the limited detection capabilities in the ultraviolet (UV) range as shown in Fig. 9.

The lower sensitivity observed for nitrogen, sulfur, and the halogens (highlighted in light orange) is attributed to the unique atomic structure of these elements. This is primarily due to their high ionization energies and significant energy gaps between electronic levels, which restrict the occurrence of observable transitions to levels with high excitation energy. Consequently, the population number densities of upper levels, and thus the line emission intensities, are inherently low for these elements.

Detection limits are connected to the standard deviation of the background signal (see equation 2), which generally decreases as the number of emitted photons increases, as illustrated in the following equation[63]:

$$\sigma_{bg} \propto \frac{1}{\sqrt{n_{ph}}}, \quad (3)$$

Where n_{ph} represents the number of photons captured by a detection system. The number of photons increases proportionally to three factors:

- The observation solid angle of the plasma,

- The detection sensitivity at the specific wavelength,

- The number of ablation occurrences used to acquire the signal.

Increasing the number of photons through the use of an optically optimized system is expected to improve the detection limits for all elements by at least one order of magnitude, compared to the LIBS apparatus used in the current experiment.

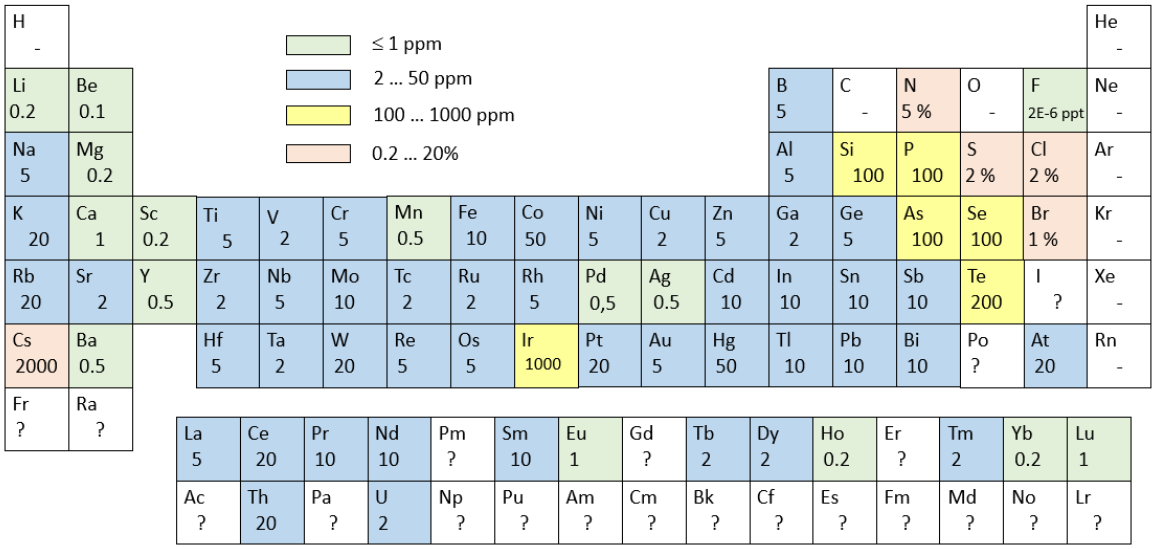

Fig. 8 Limits of detection in ppm mass fraction units for elements in diatomite. The values correspond to measurements with the spectral lines of highest analytical performance. The sensitivity available for each element is indicated by the colors. Matrix elements, rare gases, and elements with missing spectroscopic data were excluded from the analysis (white colored).

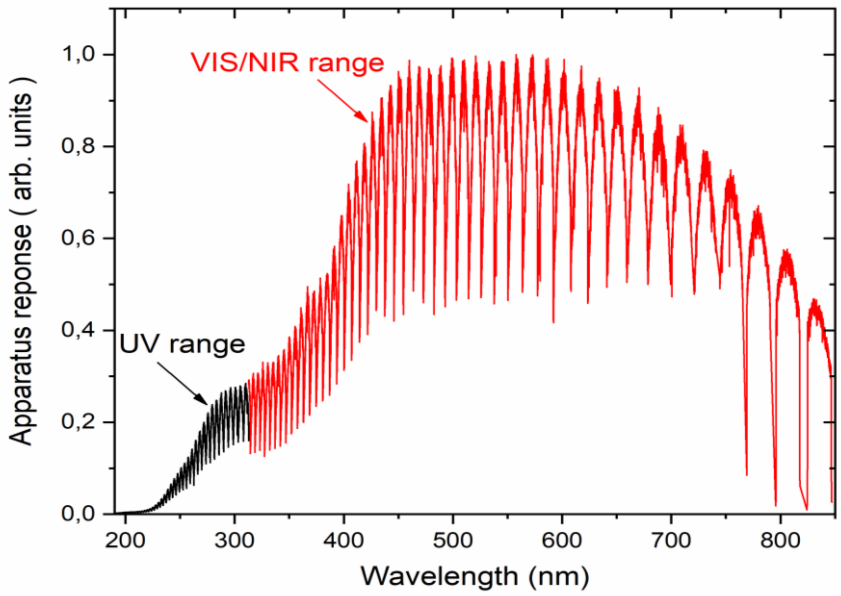

Fig. 9 Apparatus response function for the ultraviolet and visible/near infrared spectral ranges of the used echelle spectrometer (Lasertechnik Berlin, model Aryelle Butterfly).

The experimental setup employed in this study was specifically designed for calibration-free LIBS measurements conducted under controlled atmospheric conditions. To facilitate accurate data acquisition, the apparatus is equipped with an echelle spectrometer and a large focusing distance in its observation geometry. The solid angle of observation can be determined by the following trigonometric equation[63]:

$$\Omega = \frac{\pi r^2}{f^2}, \tag{4}$$

where r is the radius – i.e., half the diameter – of the lens used for capturing the plasma emission, and f represents the focal length. By employing a lens with a focal length three times shorter (f = 50 mm instead of f = 150 mm), the solid angle of observation and consequently the number of captured photons can be enhanced by nearly one order of magnitude due to the non-hemispherical, but rather elliptical shape of the laser-induced plasma. Moreover, the captured plasma emission is transported through an optical fiber with a core diameter of 600 µm to reach the echelle spectrometer. According to the entrance hole of the spectrometer, which measures 50 x 50 µm^2, approximately 1% of the captured plasma photons can enter the spectrometer. However, this loss can be avoided by implementing an optimized optical detection system (e.g. geometric collection configurations, shorter focal length, plasma coupling schemes: direct plasma coupled system & fiber-coupled system for the plasma collection…). By incorporating both improvements, the number of detected photons can be increased by a factor of 10^3.

A significant improvement in sensitivity can also be achieved by using a spectrometer equipped with diffraction gratings matched to the emission wavelength and a detector optimized for efficiency at that specific wavelength[63]. Assuming the utilization of a detection system that results in an apparatus response R_{app} as shown in Fig. 8 close to unite, the sensitivity can be further improved, and this enhancement scales as $1/R_{app}$. The achievable limits of detection C_{LOD}, given in mass fraction units, with such improved sensitivity can be deduced from the following equation by using the spectroscopic data listed in table 5:

$$C_{LOD_{optimized}} \approx \frac{C_{LOD_{measured}}}{\sqrt{\frac{1}{R_{app}} \times 1000}} \tag{5}$$

Table 5 Limit of detection C_{LOD} in mass fraction units, analytical transition, apparatus response R_{app}.

	Element	C_{LOD} (ppm)	Transition	R_{app}
Ag	Silver	0.5	Ag I 328.06	0.19
Al	Aluminum	5	Al I 396.15	0.57
As	Arsenic	100	As I 243.72	0.054
At	Astatine	20	At I 216.22	0.0046
Au	Gold	5	Au I 267.59	0.17
B	Boron	5	B I 249.77	0.065
Ba	Barium	0.5	Ba II 455.40	0.60
Be	Beryllium	0.1	Be II 313.04	0.29
Bi	Bismut	10	Bi I 293.86	0.17
Br	Bromine	1 %	Br I 635.07	0.88
Ca	Calcium	1	Ca II 393.36	0.45
Cd	Cadmium	10	Cd I 228.80	0.014
Ce	Cerium	20	Ce II 418.65	0.75
Cl	Chlorine	2 %	Cl I 837.59	0.42
Co	Cobalt	50	Co II 228.61	0.015
Cr	Chromium	5	Cr II 283.56	0.24
Cs	Cesium	2000	Cs I 584.51	0.92
Cu	Copper	2	Cu I 324.75	0.27
Dy	Dysprosium	2	Dy II 353.17	0.27
Er	Erbium	--	--	--
Eu	Europium	1	Eu II 664.5	0.8
F	Fluorine	2×10^{-6} ppm	F I 685.6	0.8
Fe	Iron	10	Fe II 259.93	0.11
Fr	Francium	--	--	--
Ga	Galium	2	Ga I 294.36	0.16
Gd	Gadolinium	--	--	--
Ge	Germanium	5	Ge I 265.11	0.076
Hf	Hafnium	5	Hf II 339.97	0.28
Hg	Mercury	50	Hg I 253.65	0.097
Ho	Holmium	0.2	Ho II 341.64	0.25
I	Iodine	--	--	--
In	Indium	10	In I 325.6	0.31
Ir	Iridium	1000	Ir II 212.68	0.006
K	Potassium	20	K I 769.89	0.5
La	Lanthanum	5	La II 394.91	0.44
Li	Lithium	0.2	Li I 670.77	0.88
Lu	Lutetium	1	Lu II 261.54	0.12
Mg	Magnesium	0.2	Mg II 279.55	0.22
Mn	Manganese	0.5	Mn II 259.37	0.078
Mo	Molybdenum	10	Mo I 317.03	0.3
N	Nitrogen	5%	N I 746.83	0.6
Na	Sodium	5	Na I 588.99	0.91
Nb	Niobium	5	Nb II 316.33	0.28
Nd	Neodymium	10	Nd II 401.22	0.44
Ni	Nickel	5	Ni I 341.47	0.25
Os	Osmium	5	Os II 321.33	0.304
P	Phosphorus	100	P I 253.56	0.095
Pb	Lead	10	Pb I 405.78	0.66
Pd	Palladium	0.5	Pd I 342.12	0.18
Pm	Promethium	--	--	--
Po	Polonium	--	--	--
Pr	Praseodymium	10	Pr II 406.28	0.62
Pt	Platinum	20	Pt I 270.23	0.12
Ra	Radium	--	--	--
Rb	Rubidium	20	Rb I 780.02	0.64
Re	Rhenium	5	Re II 337.9	0.23
Rh	Rhodium	5	Rh I 343.48	0.28
Ru	Ruthenium	2	Ru II 271.24	0.19
S	Sulfur	2 %	S I 675.71	0.76

Sb	Antimony	10	Sb I 276.99	0.15
Sc	Scandium	0.2	Sc II 361.38	0.42
Se	Selenium	100	Se I 203.98	0.0047
Si	Silicium	100	Si I 390.55	0.56
Sm	Samarium	10	Sm II 373.91	0.41
Sn	Tin	10	Sn I 326.23	0.31
Sr	Strontium	2	Sr II 407.77	0.42
Ta	Tantalum	2	Ta II 301.25	0.26
Tb	Terbium	2	Tb II 365.88	0.43
Tc	Technetium	2	Tc II 260.99	0.14
Te	Tellurium	200	Te I 214.28	0.00504
Th	Thorium	20	Th II 325.62	0.3
Ti	Titanium	5	Ti II 334.94	0.32
Tl	Thallium	10	Tl I 351.92	0.3
Tm	Thulium	2	Tm II 342.5	0.21
U	Uranium	2	U II 385.46	0.49
V	Vanadium	2	V II 310.23	0.27
W	Tungsten	20	WI 294.43	0.17
Y	Yttrium	0.5	Y II 371.02	0.43
Yb	Ytterbium	0.2	Yb II 328.93	0.25
Zn	Zinc	5	Zn I 213.85	0.0042
Zr	Zirconium	2	Zr II 339.19	0.306

The optimized limits of detections $C_{LOD_{optimized}}$ are displayed in Fig. 10.

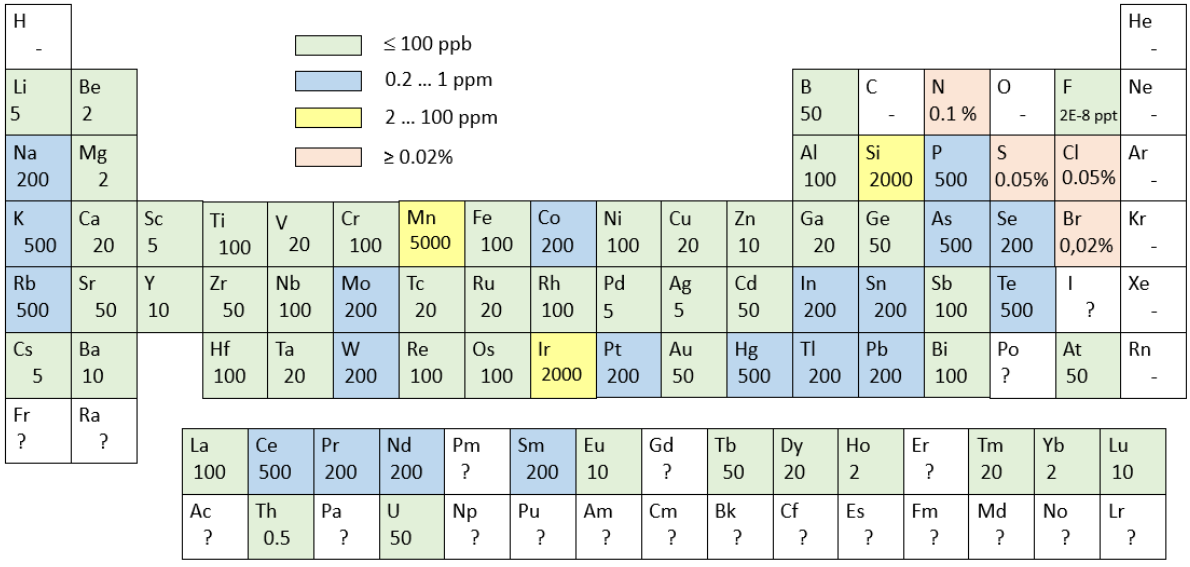

Fig. 10 Limits of detection $C_{LOD_{optimized}}$ in ppb mass fraction units being achievable with a sensitivity-improved LIBS apparatus.

By implementing a high-throughput optical system to enhance sensitivity, it is possible to improve the reported limits of detection by one or two orders of magnitude. This substantial enhancement would enable comprehensive quality control of diatomite or any other material, allowing detection and analysis of nearly all impurity elements.

4. Conclusion

The current study shows that elemental analysis of diatomite can be achieved using laser-induced breakdown spectroscopy without needing calibration with standard samples. This analysis is achieved using sensitivity-improved calibration-free LIBS that enables the measurement of the entire composition including major, minor and trace elements. Plasma emission spectra obtained during laser ablation were compared to the spectral radiance calculated for a plasma in local thermodynamic equilibrium. By applying an iterative calculation algorithm, the relative elemental fractions and plasma properties were determined from the best match between the measured and computed spectra.

Meanwhile, the use of Scanning Electron Microscopy analysis enriches this study by providing remarkable SEM images of diatomite. These images highlight the crucial role of diatomite morphology in thermal and mechanical pretreatments for silica extraction, which is of significant importance in the photovoltaic field. Furthermore, the complementary Energy-Dispersive X-ray analysis provide information on the local fluctuation of elemental fraction on a microscopic scale.

The analytical performance of LIBS is illustrated by the comparison of the measured elemental fractions for diatomite to the values obtained by XRF in literature. The mass fractions of most oxides measured by LIBS are in agreement with one or more values found in literature.

The sensitivity of LIBS detection towards diatomite was improved as shown by the detection of SrO, B_2O_3, Li_2O, and CuO, which were not detected by other methods.

We were able to evaluate the sensitivity of the LIBS measurement for 62 elements of the periodic table. By comparing the calculated intensity of the analytical transitions with the standard deviation of the continuum emission in the measured spectrum, we could moreover determine the detection limits not only for the observed minerals but also for the undetected elements.

By implementing a high-throughput optical system to enhance sensitivity, it is possible to improve the reported limits of detection by one or two orders of magnitude. This substantial enhancement would enable comprehensive quality control of diatomite, allowing detection and analysis of nearly all impurity elements.

Finally, the LIBS technique turns out to be a promising technique for the analysis and quantification of diatomaceous earth.

Conflicts of interest

There are no conflicts to declare.

Data availability

The data supporting this article have been included as part of the Supplementary Information.

Acknowledgements

The research leading to these results has received funding European Union's Horizon 2020 research and innovation programme under grant agreement No. 871124 Laserlab- Europe (projects CNRS-LP3 19948).

References

1. S. Glunz, R. Preu and D. Biro, *Comprehensive renewable energy*, 2012, **1**, 353-387.
2. A. M. Oni, A. S. Mohsin, M. M. Rahman and M. B. H. Bhuian, *Energy Reports*, 2024, **11**, 3345-3366.
3. C. J. Dawes, *Marine botany*, John Wiley & Sons, 1998.
4. A. McQuatters-Gollop, P. C. Reid, M. Edwards, P. H. Burkill, C. Castellani, S. Batten, W. Gieskes, D. Beare, R. R. Bidigare and E. Head, *Nature*, 2011, **472**, E6-E7.
5. F. E. Round, R. M. Crawford and D. G. Mann, *Diatoms: biology and morphology of the genera*, Cambridge university press, 1990.
6. R. Ragni, S. R. Cicco, D. Vona and G. M. Farinola, *Advanced Materials*, 2018, **30**, 1704289.
7. J. Davis, A. Rohatgi, R. H. Hopkins, P. D. Blais, P. Rai-Choudhury, J. R. Mccormick and H. Mollenkopf, *IEEE Transactions on electron devices*, 1980, **27**, 677-687.
8. G. Coletti, P. C. Bronsveld, G. Hahn, W. Warta, D. Macdonald, B. Ceccaroli, K. Wambach, N. Le Quang and J. M. Fernandez, *Advanced Functional Materials*, 2011, **21**, 879-890.
9. D. Macdonald and A. Cuevas, *Progress in Photovoltaics: Research and Applications*, 2000, **8**, 363-375.
10. M. Bessho, Y. Fukunaka, H. Kusuda and T. Nishiyama, *Energy and Fuels*, 2009, **23**, 4160-4165.
11. E. A. Mohamed, A. Q. Selim, A. M. Zayed, S. Komarneni, M. Mobarak and M. K. Seliem, *Journal of Colloid and Interface Science*, 2019, **534**, 408-419.
12. R. Nagahata, Y. Mori, Y. Saito, K. Takeuchi, Y. Shimizu, M. Shimizu and R. Benioub, *Materials Chemistry and Physics*, 2021, **257**, 123744.
13. G. E. Swann and S. Patwardhan, *Climate of the Past*, 2011, **7**, 65-74.
14. B. Tesson, M. J. Genet, V. Fernandez, S. Degand, P. G. Rouxhet and V. Martin-Jézéquel, *ChemBioChem*, 2009, **10**, 2011-2024.
15. N. Marín-Alzate, J. I. Tobón, B. Bertolotti, M. E. Q. Cáceda and E. Flores, *Water, Air, and Soil Pollution*, 2021, **232**, 122.
16. H. A. A. L. Saoud, M. Sprynskyy, R. Pashaei, M. Kawalec, P. Pomastowski and B. Buszewski, *Journal of Separation Science*, 2022, **45**, 3362-3376.
17. I. Abdellaoui, M. M. Islam, T. Sakurai, S. Hamzaoui and K. Akimoto, *Hydrometallurgy*, 2018, **179**, 207-214.
18. D. W. Hahn and N. Omenetto, *Applied spectroscopy*, 2012, **66**, 347-419.
19. F. J. Fortes, J. Moros, P. Lucena, L. M. Cabalín and J. J. Laserna, *Analytical chemistry*, 2013, **85**, 640-669.
20. I. B. Gornushkin, L. A. King, B. W. Smith, N. Omenetto and J. D. Winefordner, *Spectrochimica Acta Part B: Atomic Spectroscopy*, 1999, **54**, 1207-1217.
21. C. Aragon, J. Bengoechea and J. A. Aguilera, *Spectrochimica Acta Part B: Atomic Spectroscopy*, 2001, **56**, 619-628.
22. A. Taleb, V. Motto-Ros, M. J. Carru, E. Axente, V. Craciun, F. Pelascini and J. Hermann, *Analytica Chimica Acta*, 2021, **1185**, 339070.
23. A. Ciucci, M. Corsi, V. Palleschi, S. Rastelli, A. Salvetti and E. Tognoni, *Applied spectroscopy*, 1999, **53**, 960-964.
24. E. Tognoni, G. Cristoforetti, S. Legnaioli, V. Palleschi, A. Salvetti, M. Müller, U. Panne and I. Gornushkin, *Spectrochimica Acta Part B: Atomic Spectroscopy*, 2007, **62**, 1287-1302.
25. V. Lazic, R. Barbini, F. Colao, R. Fantoni and A. Palucci, *Spectrochimica Acta Part B: Atomic Spectroscopy*, 2001, **56**, 807-820.
26. D. Bulajic, M. Corsi, G. Cristoforetti, S. Legnaioli, V. Palleschi, A. Salvetti and E. Tognoni, *Spectrochimica Acta Part B: Atomic Spectroscopy*, 2002, **57**, 339-353.
27. A. El Sherbini, T. M. El Sherbini, H. Hegazy, G. Cristoforetti, S. Legnaioli, V. Palleschi, L. Pardini, A. Salvetti and E. Tognoni, *Spectrochimica Acta Part B: Atomic Spectroscopy*, 2005, **60**, 1573-1579.
28. J. Hermann, Patent **US8942927B2**, United States, 2015.
29. J. Hermann, C. Boulmer-Leborgne and D. Hong, *Journal of applied physics*, 1998, **83**, 691-696.
30. C. Gerhard, J. Hermann, L. Mercadier, L. Loewenthal, E. Axente, C. R. Luculescu, T. Sarnet, M. Sentis and W. Viöl, *Spectrochimica Acta Part B: Atomic Spectroscopy*, 2014, **101**, 32-45.
31. J. Hermann, E. Axente, F. Pelascini and V. Craciun, *Analytical chemistry*, 2019, **91**, 2544-2550.
32. C. Gerhard, A. Taleb, F. Pelascini and J. Hermann, *Applied Surface Science*, 2021, **537**, 147984-147984.
33. C. T. Chen, D. Banaru, T. Sarnet and J. Hermann, *Spectrochimica Acta - Part B Atomic Spectroscopy*, 2018, **150**, 77-85.
34. J. Hermann, *Laser Induced Breakdown Spectroscopy (LIBS) Concepts, Instrumentation, Data Analysis and Applications*, 2023, **1**, 89-121.
35. R. van Vleck Anderson, *The Journal of Geology*, 1933, **41**, 673-698.
36. W. Yang, P. J. Lopez and G. Rosengarten, *Analyst*, 2011, **136**, 42-53.

37. J. R.Rosowski, *CAN,J,MICROBIOL*, 1992, **38**, 676-686.
38. X. Chen, C. Wang, E. Baker and C. Sun, *Scientific reports*, 2015, **5**, 11977.
39. D. Losic, *Diatom nanotechnology: progress and emerging applications*, Royal Society of Chemistry, 2018.
40. T. Fuhrmann, S. Landwehr, M. El Rharbi-Kucki and M. Sumper, *Applied Physics B*, 2004, **78**, 257-260.
41. C. Jeffryes, J. Campbell, H. Li, J. Jiao and G. Rorrer, *Energy and Environmental Science*, 2011, **4**, 3930-3941.
42. J. Toster, K. S. Iyer, W. Xiang, F. Rosei, L. Spiccia and C. L. Raston, *Nanoscale*, 2013, **5**, 873-876.
43. M. Hakamada, Y. Fukunaka, T. Oishi, T. Nishiyama and H. Kusuda, *Metallurgical and Materials Transactions B: Process Metallurgy and Materials Processing Science*, 2010, **41**, 350-358.
44. T. Homma, N. Matsuo, X. Yang, K. Yasuda, Y. Fukunaka and T. Nohira, *Electrochimica Acta*, 2015, **179**, 512-518.
45. M. Cirisan, M. Cvejić, M. R. Gavrilović, S. Jovićević, N. Konjević and J. Hermann, *Journal of Quantitative Spectroscopy and Radiative Transfer*, 2014, **133**, 652-662.
46. M. Burger and J. Hermann, *Spectrochimica Acta - Part B Atomic Spectroscopy*, 2016, **122**, 118-126.
47. A. Kramida, Y. Ralchenko, J. Reader and NIST ASD Team, NIST Atomic Spectra Database, version 5.11, 2023, *Journal*, 2023, https://physics.nist.gov/asd
48. N. Konjevic and J. R. Roberts, *Journal of Physical and Chemical Reference Data*, 1976, **5**, 209-257.
49. N. Konjević and W. L. Wiese, *Journal of Physical and Chemical Reference Data*, 1990, **19**, 1307-1385.
50. F. Colao, R. Fantoni, V. Lazic, A. Paolini, F. Fabbri, G. G. Ori, L. Marinangeli and A. Baliva, *Planetary and Space Science*, 2004, **52**, 117-123.
51. J. Osán, I. Szalóki, C.-U. Ro and R. Van Grieken, *Microchimica Acta*, 2000, **132**, 349-355.
52. A. Laskin, J. P. Cowin and M. J. Iedema, *Journal of Electron Spectroscopy and Related Phenomena*, 2006, **150**, 260-274.
53. M. Scimeca, S. Bischetti, H. K. Lamsira, R. Bonfiglio and E. Bonanno, *European journal of histochemistry: EJH*, 2018, **62**, 2841.
54. S. J. B. Reed, *Electron microprobe analysis and scanning electron microscopy in geology*, Cambridge university press, 2005.
55. F. Georget, J. Schmatz, E. Wellmann and T. Matschei, *Journal of Microscopy*, 2024, **294**, 105-116.
56. E. Manova, P. Aranda, M. Angeles Martín-Luengo, S. Letaïef and E. Ruiz-Hitzky, *Microporous and Mesoporous Materials*, 2010, **131**, 252-260.
57. R. Cherrak, M. Hadjel and N. Benderdouche, *Oriental Journal of Chemistry*, 2015, **31**, 1611-1620.
58. M. Safa, M. Larouci, B. Meddah and P. Valemens, *Water Science and Technology*, 2012, **65**, 1729-1737.
59. A. Touina, S. Chernai, B. Mansour, H. Hadjar, A. Ouakouak and B. Hamdi, *SN Applied Sciences*, 2021, **3**, 476.
60. A. A. Reka, B. Pavlovski, B. Boev, S. Bogoevski, B. Boškovski, M. Lazarova, A. Lamamra, A. Jashari, G. Jovanovski and P. Makreski, *Geologica Macedonica*, 2021, **35**, 5-14.
61. A. F. Danil de Namor, A. El Gamouz, S. Frangie, V. Martinez, L. Valiente and O. A. Webb, *Journal of Hazardous Materials*, 2012, **241-242**, 14-31.
62. Analytical Methods Committee, *Analyst*, 1987, **112**, 199-204.
63. L. Casanova, S. A. Beldjilali, G. Bilge, B. Sezer, V. Motto-Ros, F. Pelascini, D. Bănaru and J. Hermann, *Spectrochimica Acta - Part B Atomic Spectroscopy*, 2023, **207**, 106760.